Journal of Colloid and Interface Science 566 (2020) 271–283

Contents lists available at ScienceDirect

Journal of Colloid and Interface Science

journal homepage: www.elsevier.com/locate/jcis

Developing highly nanoporous titanate structures *via* wet chemical conversion of DC magnetron sputtered titanium thin films

Matthew D. Wadge [a,*], Burhan Turgut [a], James W. Murray [a], Bryan W. Stuart [a], Reda M. Felfel [a,b], Ifty Ahmed [a], David M. Grant [a,*]

[a] Advanced Materials Research Group, Faculty of Engineering, University of Nottingham, UK
[b] Physics Department, Faculty of Science, Mansoura University, Mansoura, Egypt

GRAPHICAL ABSTRACT

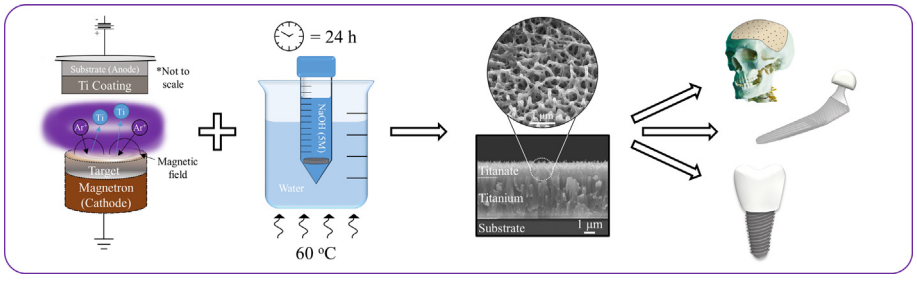

ARTICLE INFO

Article history:
Received 8 October 2019
Revised 13 January 2020
Accepted 19 January 2020
Available online 22 January 2020

Keywords:
Conversion coating
DC magnetron sputtering
Titanate
Bioactive
Nanoporous

ABSTRACT

Titanate structures have been widely investigated as biomedical component surfaces due to their bioactive, osteoinductive and antibacterial properties. However, these surfaces are limited to Ti and its alloys, due to the nature of the chemical conversion employed. The authors present a new method for generating nanoporous titanate structures on alternative biomaterial surfaces, such as other metals/alloys, ceramics and polymers, to produce bioactive and/or antibacterial properties in a simple yet effective way. Wet chemical (NaOH; 5 M; 60 °C; 24 h) conversion of DC magnetron sputtered Ti surfaces on 316L stainless steel were investigated to explore effects of microstructure on sodium titanate conversion. It was found that the more equiaxed thin films (B/300) generated the thickest titanate structures (*ca.* 1.6 µm), which disagreed with the proposed hypothesis of columnar structures allowing greater NaOH ingress. All film parameters tested ultimately generated titanate structures, as confirmed *via* EDX, SEM, XPS, XRD, FTIR and Raman analyses. Additionally, the more columnar structures (NB/NH & B/NH) had a greater quantity of Na (*ca.* 26 at.%) in the top portion of the films, as confirmed *via* XPS, however, on average the Na content was consistent across the films (*ca.* 5–9 at.%). Film adhesion for the more columnar structures (*ca.* 42 MPa), even on polished substrates, were close to that of the FDA requirement for plasma-sprayed HA coatings (*ca.* 50 MPa). This study demonstrates the potential of these surfaces to be applied onto a wide variety of material types, even polymeric materials, due to the lower processing temperatures utilised, with the vision to generate bioactive and/or antibacterial properties on a plethora of bioinert materials.

1. Introduction

Medical implants' reliance on extracellular tissue growth, is fundamentally restricted by the success of the surface modification

* Corresponding authors.
E-mail addresses: matthew.wadge@nottingham.ac.uk (M.D. Wadge), david.grant@nottingham.ac.uk (D.M. Grant).

https://doi.org/10.1016/j.jcis.2020.01.073
0021-9797/

used to enhance their inherently bioinert surfaces. Despite titanium (Ti) and its alloys' (specifically Ti-6Al-4V) advantages regarding corrosion resistance, and their minimal allergenic and immunogenic potential compared to previously used cobalt-chrome (Co-Cr-Mo) alloys or 316L stainless steel (SS), they require sufficient modification to ensure a more natural adhesion (integration mechanically and chemically achieved through bone ingrowth rather than through cementation) at the implant-tissue interface [1].

Presently, surface modification of metallic implants used clinically is performed exclusively by coating (in line with the Food and Drug Administration's (FDA) regulatory processes) with hydroxyapatite (HA) through high-temperature (>15,000 K plasma temperature [2]; >1500 K droplet temperature [3]) plasma spraying methodologies [4]. By propelling molten particles, generated *via* injection of powder through a plasma torch, towards the implant surface, a coating forms through rapid quenching and solidification. However, this process causes residual stresses and crystallisation within the produced coating [5], and can often modify the underlying substrate. Over time, the residual stresses encourage propagation of micro-cracks, thereby reducing the long-term stability of the coating *in vivo*. This can lead to delamination and particle formation which, in turn, can lead to loosening of the implant [6].

An alternative methodology, which aimed to circumvent the issues with plasma spraying, was developed by Kokubo et al. [7–9]. Bioactive titanates (particularly sodium titanate; $Na_2Ti_xO_{2x+1}$, $x = 1, 2, 3\cdots$), which are generated through simple wet-chemical routes at much lower processing temperatures (60 °C), demonstrated tailorability through cationic exchange, as well as nanoporous morphology for potential bone ingrowth. By facilitating ion-exchange reactions *in vitro* and *in vivo*, apatite formation was possible, enabling natural adhesion at the implant-tissue interface, with successful clinical deployment in 10,000 patients in Japan (98% implant survivorship 10 years post-implantation [10]). Titanate surfaces have also been considered for antibacterial applications due to their ion-exchangeability, with silver (Ag) (Lee et al. [11]) and more recently gallium (Ga) (Wadge et al. [12] and Yamaguchi et al. [13]), to facilitate a two-in-one bioactive and antibacterial surface, being notable examples.

Translation of these surfaces on alternative substrate materials (other metals/alloys, polymers, and ceramics), however, has been limited, specifically in the biomedical sector. Various research groups have investigated reactive magnetron sputtering of titanate structures [14], however no research investigating wet-chemical conversion of direct current (DC) magnetron sputtered Ti thin films has yet been published. The overall aim of our research is to develop this technology for a wide range of biomaterials, enabling functionalisation of surfaces tailored to specific applications. The wet chemical method used, as outlined by Kokubo and his team [7–9], relies upon substrate submersion in concentrated (>5 M) sodium hydroxide (NaOH), enabling simplistic and low energy production of sodium titanate structures. This technique is appropriate for the intended application, since it is scalable, enables full conversion of complex geometries, is not energy intensive and does not require complicated costly equipment. The objectives of this study were to investigate the effect of initial surface parameters (film density, structure factor etc.) on the wet-chemical conversion to titanate structures, and explore the possibility of producing titanate structures on alternative biomedical materials.

2. Methodology

2.1. Substrate preparation

316L stainless steel (SS) discs (1 mm thick; 10 mm diameter; >99.9% purity; Smiths Metals Ltd., Nottingham) were polished using abrasive silicon carbide (SiC) paper, with sequentially higher grit from P240 to P4000, followed by colloidal silica polishing (*ca.* 0.06 μm particle size) on MD-Chem polishing pads. Polished fused silica discs were utilised for surface and cross-sectional SEM observations. The discs were then cleaned ultrasonically in acetone (99.8% purity, Honeywell), followed by Industrial Methylated Spirit (IMS, purity 99.9%, Sigma-Aldrich) for 10 min each, and subsequently air dried, prior to sputtering.

2.2. DC magnetron sputtering

To produce the Ti thin films, a TEER UDP-650 type 2 unbalanced magnetron sputtering rig was used, fitted with a solid Ti target (>99.6% purity; 175 × 380 mm, Teer Coatings Ltd.). All substrates were fixed to a rotating sample holder using double-sided polyimide Kapton tape, with samples mounted at a set substrate to target distance (55 ± 1 mm) and were rotated at 5 RPM. Initially, the chamber was pumped down using consecutive rotary and diffusion pumping stages to a base vacuum of $<1 \times 10^{-5}$ Torr, before introducing Ar gas (purity 99.999%; Pureshield BOC©) at a rate of 20 standard cubic cm/min (sccm). Prior to deposition, all samples were bias cleaned using a pulsed DC bias at a pulse width of 250 kHz, a step time of 500 ns, and a bias voltage of −100 V for 15 min. Various processing parameters were varied to induce structural difference in the produced Ti films, however, target power density was maintained at 2.38 W cm^{-2} (5 A, −300 V) to minimise sputtering times. Two parameters that were varied during the sputtering process; the applied bias to the substrates (either 0 or −100 V) and substrate temperature, which was controlled using a mounted heater within the vacuum chamber, it was either off or operated at 150 or 300 °C. Processing parameters and matching sample codes are shown in Table 1.

2.3. Sodium hydroxide chemical treatment

A *ca.* 5 M NaOH solution was prepared using NaOH pellets (*ca.* 19.99 g per 100 mL of distilled water; 99.9% purity; Sigma-Aldrich). 10 mL aliquots were then dispensed into polypropylene containers, with individual discs suspended in each. These were then sealed and heated in a low temperature furnace at 60 ± 2 °C for 24 h. Upon removal, samples were washed in deionised water for 60 s, before compressed air drying followed by storage within a desiccator until testing.

Table 1
Coating parameters used for deposition of Ti films (*ca.* 4 μm thickness) with varying degrees of density/porosity. Sample codes are explained as follows: NB/NH = no bias and no applied heating; B/NH = −100 V bias and no applied heating; B/150 = −100 V bias and 150 °C heating; B/300 = −100 V bias and 300 °C heating.

Sample Code	Target Current/A	Substrate Bias/V	Substrate Heating/°C	Coating Time/min	Calculated Sputtering Rate/nm min^{-1}
NB/NH	5	0	0	263	14.8 ± 0.11
B/NH	5	−100	0	278	14.0 ± 0.12
B/150	5	−100	150	278	13.3 ± 0.15
B/300	5	−100	300	278	13.2 ± 0.08

2.4. Materials characterisation

2.4.1. Scanning electron microscopy (SEM) and energy dispersive X-ray spectroscopy (EDX)

Scanning electron micrographs and surface compositional analysis were obtained using a JEOL 7100F Field-Emission Gun Scanning Electron Microscope (FEG-SEM) with an attached Energy Dispersive X–ray (EDX) Spectrometer (Oxford Instruments). A working distance of 10 mm was maintained with acquisitions utilising a beam voltage of 15 kV. Qualitative pore/void area and frequency analysis was conducted using the 'analyse particle' plugin in ImageJ, from high contrast SEM images for good accuracy, with a threshold set at *ca.* 45%.

Cross-sectional SEM was conducted to determine the thickness of all converted and unconverted layer thicknesses, with error measurements taken from 5 separate areas, with 3 replicate measurements taken for each area (n = 15). Fused silica discs were utilised for these measurements, as shattering of the discs using a diamond-tipped scribe enabled clear imaging of the cross-sectional morphology. Statistical significance was calculated using a one-way analysis of variance (ANOVA) assessment.

2.4.2. Focussed ion-beam scanning electron microscopy (FIB-SEM)

FIB-SEM was used to mill out sections of the sample for further cross-sectional analysis. An FEI Quanta 200 3D (FEI, Portland, OR) system was used, with Ga^+ ion milling performed at 30 kV, and currents ranging from 1 nA to 30 pA. Standard FEI gas injectors were used to deposit platinum (Trimethyl(methylcyclopentadienyl) platinum(IV); 25 °C crucible temperature), which was introduced onto the sample *via* an internal gas injector. Samples were imaged on the JEOL 7100F FEG-SEM utilising the same parameters in Section 2.4.1, with a 40° stage tilt.

2.4.3. X-ray diffraction (XRD) and texture coefficient calculation

Crystallographic structures, particularly noting preferred orientation in specific crystallographic planes, were assessed using a Bruker D8 advance XRD spectrometer, utilising a parallel beam geometry and glancing angle beam parameters as follows: Cu Kα source; λ = 1.5406 Å; 40 kV; 35 mA. Spectra were measured over a 2θ range of 20–60°, with a step size of 0.015° (2θ), a glancing angle of 1.2°, and a dwell time of 16 s. Relative peak intensities were calculated from the raw spectral data in Bruker's DIFFRAC. EVA software, and the texture coefficient values were obtained using the Harris equation [15]:

$$T_c(h_i k_i l_i) = \left(\frac{I_m(h_i k_i l_i)}{I_0(h_i k_i l_i)}\right)\left[\frac{1}{n}\sum_{i=1}^{n}\left(\frac{I_m(h_i k_i l_i)}{I_0(h_i k_i l_i)}\right)\right]^{-1}$$

where I_m is the measured diffraction intensity, I_0 is the diffraction database intensity value, and n is the number of peaks being calculated, in this case n = 4.

2.4.4. X-ray photoelectron spectroscopy (XPS)

For X-ray Photoelectron Spectroscopic (XPS) measurements, a VG ESCALab Mark II X-ray photoelectron spectrometer with a monochromatic aluminium (Al) Kα X-ray source was utilised. Beam incidence angle was maintained at *ca.* 30°, with both survey and high-resolutions scans conducted. For calibration, high-resolution scanning of the C 1s spectral peak, charge corrected to 284.8 eV, was conducted. Acquisition parameters used were as follows: scan number = 5; dwell times of 0.2 and 0.4 s for survey and high-resolution scans, respectively; and a step size of 1 and 0.2 eV for survey and high-resolution scans, respectively. Survey scans were measured over a range of 0–1200 eV, with all scans analysed using CasaXPS software constraining all deconvoluted peaks of the same elements to the same Full Width at Half Maximum (FWHM), with additional area ratio constraints maintained for spin-orbit splitting (or *j-j* coupling).

2.4.5. Raman spectroscopy

For Raman spectroscopy measurements, a HORIBA Jobin Yvon LabRAM HR spectrometer was utilised. Beam and acquisition parameters were as follows: 532 nm laser (25 mW power); 50× objective lens; 300 μm confocal pinhole; 600 lines/mm rotatable diffraction grating with a path length of 800 mm, for simultaneous scanning of multiple Raman shifts. A SYNAPSE CCD detector (1024) pixels, thermoelectrically cooled to −60 °C, was utilised for spectra detection. Calibration of the instrument was conducted using both a standard Si (1 0 0) reference band (520.5 cm^{-1}) and the Rayleigh line (0 cm^{-1}). Spectral acquisition was conducted for 10 s, with 10 accumulations per sample.

2.4.6. Fourier transform infrared spectroscopy (FTIR)

A Bruker Tensor FTIR spectrometer with an Attenuated Total Reflectance (ATR) attachment containing a diamond crystal/ZnSe lens was used for infrared absorbance measurements. A spectral range of 4000–500 cm^{-1} wavenumber was observed and maintained for all acquisitions.

2.4.7. Surface roughness – Optical profilometry

Surface roughness quantification was conducted using focus variation microscopy performed on an Alicona Infinite Focus instrument. A 50× objective lens was used in all cases, with raw data being levelled using the least squares plane method. 3D areal surface texture parameters were extracted using the ISO 25178-2 standard [16]. A vertical resolution of 70 nm was utilised, with a horizontal resolution of 2 μm.

2.4.8. Pull off adhesion strength

The adhesion strength of sputtered Ti films was tested using a portable adhesion testing (P.A.T handy (DFD® Instruments)) unit in accordance with ASTM-D4541-17 [17]. Stubs (2.8 mm radii) were adhesively bonded to the coated samples using DFD® E1100S epoxy, which was cured for 60 min at 140 °C, and then left to cool to room temperature. All discs were cleaned with compressed air, and air bubbles formed between the stub and disc were carefully removed through pressing of the stubs. Any excess epoxy following curing was removed *via* a cylindrical cutting tool supplied with the equipment. Analysis of the failure sites was conducted using a Nikon LV100ND upright light microscope.

2.4.9. Scratch adhesion testing

Analysis of both unconverted and titanate converted coating failure was conducted in accordance to BS EN ISO 20502:2016, using a CETR UMI multiple specimen scratch testing system equipped with a Rockwell C indenter. Prior to each scratch, the indenter was cleaned with isopropyl alcohol. Modified testing regimes were utilised due to some failure modes being considerably less than the standard 30 N, making quantification difficult. Therefore, loads were applied over a distance of 3 mm, with preloading of 0.5 N and progressive loading up to a value of 15 N over a period of 180 s. The failure sites were again analysed using a Nikon LV100ND upright microscope.

3. Results

3.1. Topographical, structural and compositional analysis

3.1.1. SEM and EDX plus XPS compositional analysis

As observed in the SEM micrographs (Fig. 1A–D) the frequency (*ca.* 4.1, 3.0, 1.8, and 0.6 μm^{-2}, for NB/NH, B/NH, B/150 and B/300

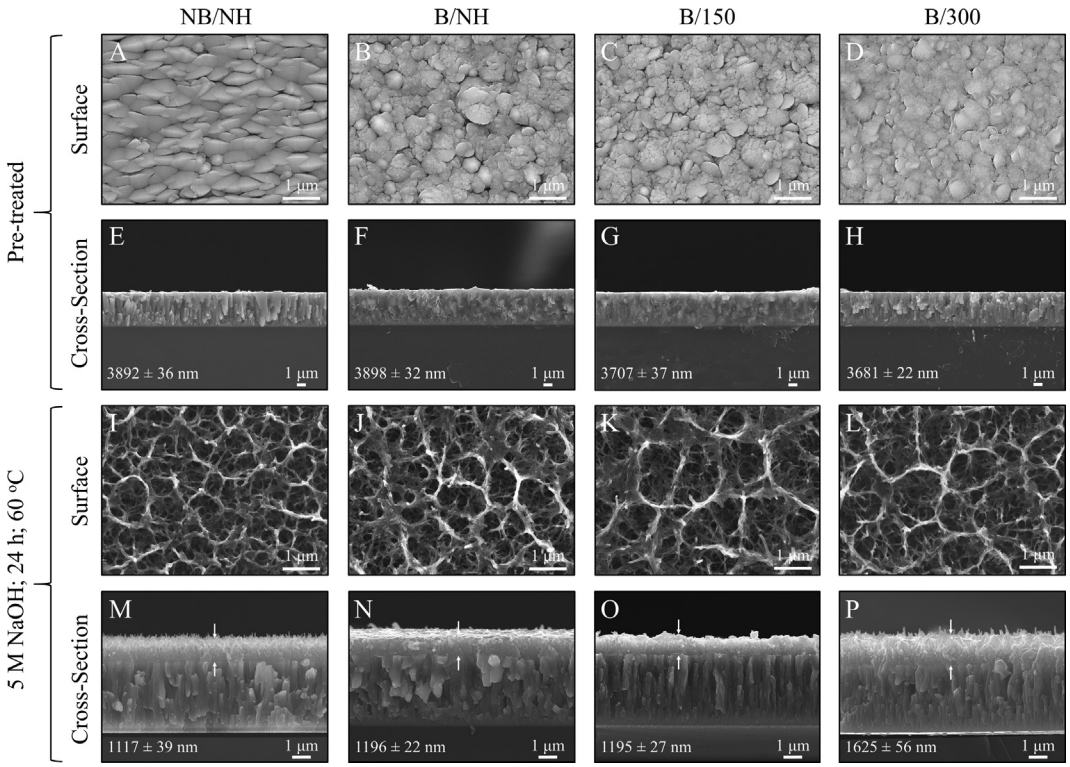

Fig. 1. SEM surface and cross-sectional micrographs for unconverted and converted DC magnetron sputtered films. (A–D) Surface micrographs of all unconverted Ti samples. (E–H) Cross-sectional images of all unconverted Ti samples. (I–L) Surface micrographs of all converted titanate samples. (M–P) Cross-sectional images of all converted samples, with arrows indicating titanate portion. Coating thickness with standard error is written in each image.

samples, respectively) and area (*ca.* 3713.7, 2541.3 1436.8, and 1028.6 nm^2, for NB/NH, B/NH, B/150 and B/300 samples, respectively) of surface voids appear to diminish from the NB/NH sample to the B/300 sample (see supplementary data Fig. S1). The sputtering time was increased from 263 min for the NB/NH sample (Fig. 1E) to 278 min for the B/NH sample (Fig. 1F) to maintain the same coating thickness (*ca.* 3.9 µm), suggesting the increased density of the coating given the similar rate of deposition. Furthermore, through the application of substrate heating at 150 and 300 °C, it is clear the thickness of the produced films at the same sputtering time decreased to *ca.* 3.7 µm for the B/150 and B/300 samples (Fig. 1G–H).

Clear surface alterations are noted for the titanate samples, with nanoporous morphologies consistent with sodium titanate surfaces (Fig. 1I–L). It is also noted that the pore size (defined as the area enclosed by the larger strutted structures) appears to increase with increasing density of the produced Ti coating, however, the large error associated with the B/150_TC sample in the supplementary data may affect its significance (see supplementary data Fig. S2). In addition to the titanium coating, the thickness of the titanate converted films were also assessed. When observing the thickness of the titanate converted portion of the Ti coating, it is evident that this region increases in depth through the application of a bias (from the NB/NH sample (*ca.* 1.12 µm) to the B/NH sample (*ca.* 1.20 µm); Fig. 1M & N), as well as the increase in substrate temperature (from the B/150 sample (*ca.* 1.20 µm) to the B/300 sample (*ca.* 1.63 µm); Fig. 1O & *P*). The increase in depth from all titanate converted samples to the B/300_TC sample is statistically significant ($p < 0.0001$), however, the increase from the NB/NH_TC, to both the B/NH_TC and B/150_TC samples exhibited no statistical significance.

Elemental analysis *via* EDX (Table 2) demonstrated similar sodium (Na) inclusion of *ca.* 7.6, 8.9, 5.6 and 7.6 at.% for the NB/NH_TC, B/NH_TC, B/150_TC, and B/300_TC samples, respectively. Both Ti and O content remained constant, with small inclusions (<1 at.%) of Ca. In comparison, elemental analysis determined *via* XPS showed a large increase in Na for all samples, with 25.6, 26.8, 16.1, and 17.8 at.% for NB/NH_TC, B/NH_TC, B/150_TC and B/300_TC, respectively. The surface composition examined by XPS showed that Ti and O content remained similar for the NB/NH_TC, B/NH_TC samples, but was higher for the B/150_TC and B/300_TC samples.

3.1.2. FIB-SEM

Additional cross-sectional information of the samples was determined *via* FEG-SEM of a FIB milled titanate converted sample. The micrograph (Fig. 2A) demonstrates clear interconnected nanoporosity, with homogenous distribution of sodium (Fig. 2C)

Table 2
EDX and XPS data of titanate converted DC magnetron sputtered Ti films. Values given with standard error values (n = 3). All unconverted samples contained 100% Ti, with titanate converted samples also containing trace amounts of Ca (<1 at.%).

Sample	EDX			XPS		
	Na/at.% (EDX)	O/at.% (EDX)	Ti/at.% (EDX)	Na/at.% (XPS)	O/at.% (XPS)	Ti/at.% (XPS)
NB/NH_TC	7.6 ± 0.1	61.0 ± 0.1	30.8 ± 0.1	25.6 ± 0.6	56.9 ± 0.6	17.5 ± 0.3
B/NH_TC	8.9 ± 0.1	57.3 ± 0.5	33.2 ± 0.6	26.8 ± 0.7	55.4 ± 0.6	17.8 ± 0.3
B/150_TC	5.6 ± 0.1	57.6 ± 0.2	36.9 ± 0.2	16.1 ± 0.4	62.4 ± 0.5	21.5 ± 0.3
B/300_TC	7.6 ± 0.1	60.1 ± 0.2	32.2 ± 0.1	17.8 ± 0.4	62.4 ± 0.5	19.9 ± 0.3

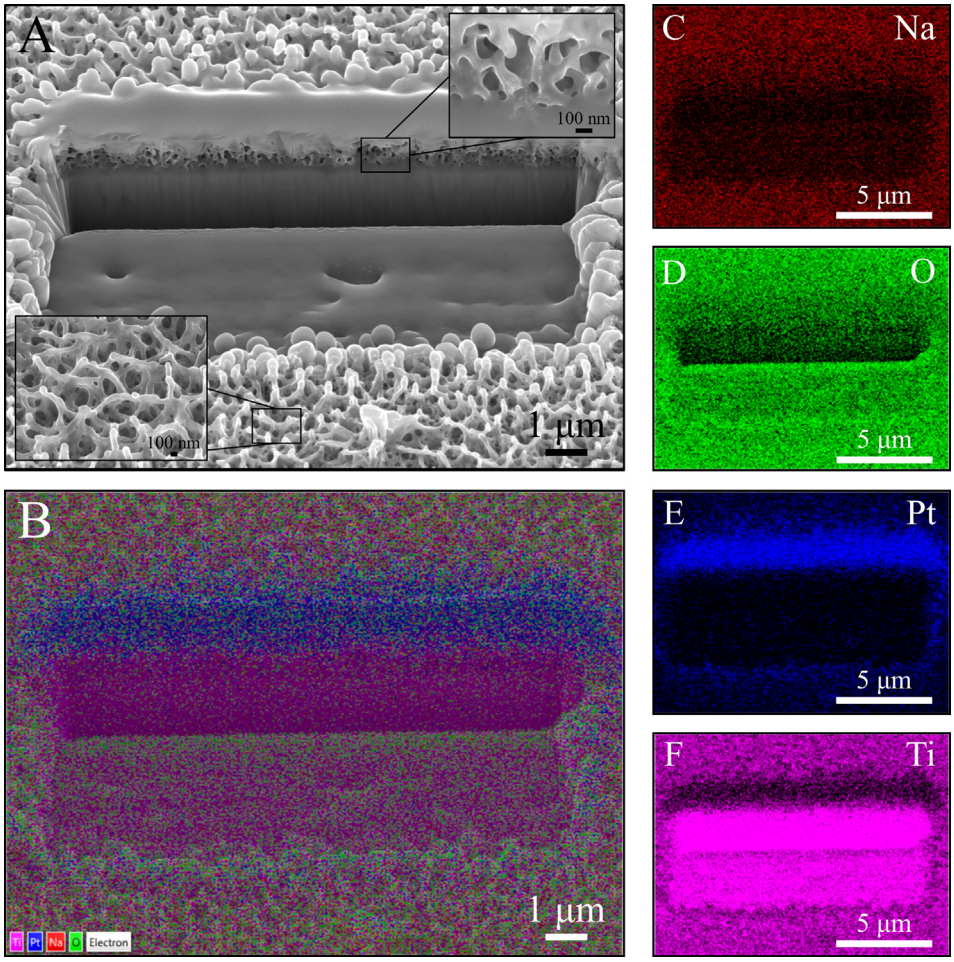

Fig. 2. (A) Representative FEG-SEM micrograph of a FIB milled titanate converted sample tilted at 40° to demonstrate the interconnected porosity and interface between the Ti thin film and the converted titanate portion (insert images show higher resolution micrographs of aforementioned features). (B) Composite EDX maps of all elements present with individual elemental maps of (C) sodium, (D) oxygen, (E) platinum (introduced from the FIB milling process), and (F) titanium.

across the surface of the sample, and homogeneous distribution of titanium within the coating (Fig. 2F). Sodium and oxygen (Fig. 2C & D) penetration appears to decrease through the through thickness of the coating. Vertical growth of the titanate struts are clear on the insert micrographs.

3.1.3. XRD and texture coefficient

XRD spectral data (Fig. 3A) demonstrated for the NB/NH sample, preferred orientation in the (0 0 2) plane of HCP Ti (PDF 00–044-1294) at 38.4° 2θ, with additional smaller peaks at 40.2° and 53.0° 2θ corresponding to the (1 0 1) and (1 0 2) planes, respectively; no other peaks were observed. However, through the application of a bias to the B/NH sample, the relative intensities of the peaks, and number of peaks increased, with a new peak at 35.2° 2θ corresponding to the (1 0 0) plane. The peak corresponding to the (1 0 1) plane increased in intensity. Continuing the trend, through application of substrate heating in both the B/150 and B/300 samples, peaks corresponding to the (1 0 0) and (1 0 1) planes saw an increase in their relative intensities, with the (1 0 1) peak having the highest relative intensity for both samples. Following titanate conversion (Fig. 3B), 3 additional broader peaks were detected on all samples at *ca.* 24.2, 28.4 and 48.2° 2θ, assigned to titanate species (PDF 00-022-1404 and PDF 00-025-1450), however direct assignment was difficult due to the amorphous nature of the peaks.

Further analysis of the change in preferred orientation was conducted through calculation of texture coefficients (T_c; Fig. 4). Using Harris' equation, the degree of preferred orientation can be numerically calculated through ratios between measured peak intensities and database intensities for the same material. A T_c of 1 would indicate an equiaxed sample equating to the material's database structure, whilst a texture coefficient of n (n being the number of peaks calculated; in this case n = 4) would indicate complete preferred orientation in that plane. For the NB/NH sample, as seen with the XRD data, the crystalline structure was preferentially orientated in the (0 0 2), with a $T_{c(0\ 0\ 2)}$ = 3.39. This value reduced to 2.66 in the B/NH sample, showing a subtle shift from the more columnar structure exhibited in the NB/NH sample. Further reductions of $T_{c(0\ 0\ 2)}$, to 2.04 and 1.54 occurred for the B/150 and B/300 samples, respectively, demonstrating further shifts from preferred orientation in the columnar grown NB/NH sample, to more equiaxed structures as $T_c \rightarrow 1$.

3.1.4. X-ray photoelectron spectroscopy (XPS)

XPS quantification showed significant differences in the high-resolution Ti 2p, O 1s, and Na 1s spectra, as well as subtle alterations in peak intensity/presence, and elemental quantities. In the survey spectra (Fig. 5A), a significant difference from the control to all Ti coated samples was noted, with consistent peak positions and peak intensities of all Ti and O photoelectron emissions. Following NaOH treatment, peaks corresponding to Na were

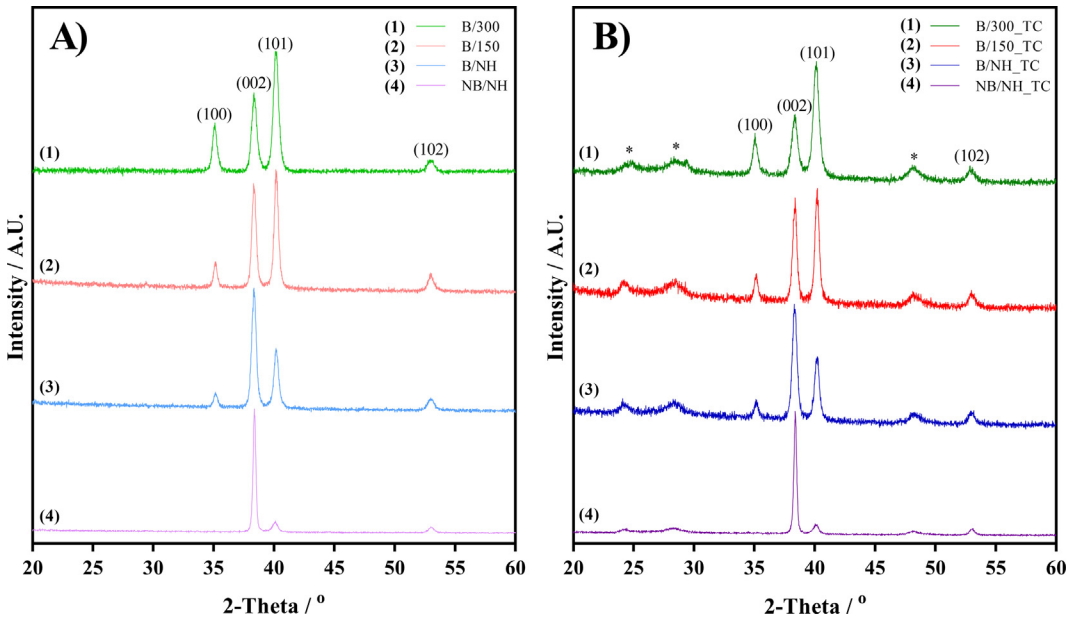

Fig. 3. XRD spectral analysis of unconverted Ti (A) and titanate converted (B) samples. Deconvolution of Ti peaks correspond to HCP Ti (PDF 00-044-1294), with * indicating additional peaks, attributed to titanate species (PDF 00-022-1404 and PDF 00-025-1450), which were not found in the unconverted samples.

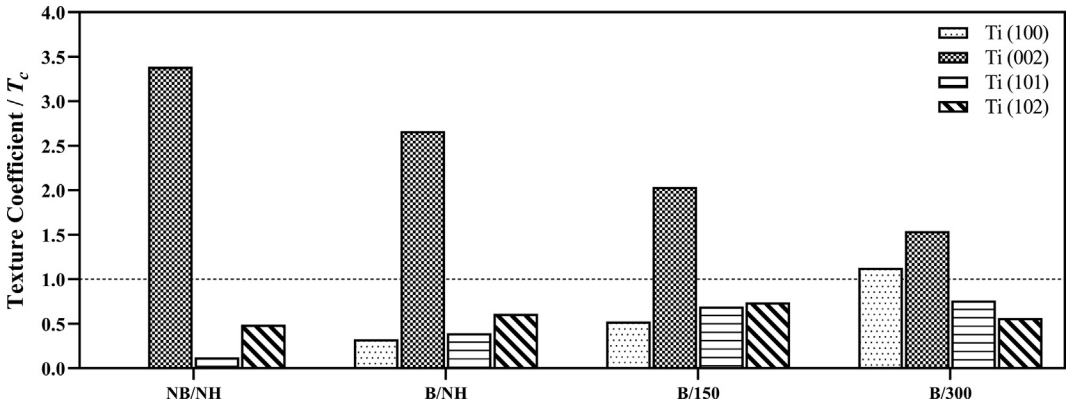

Fig. 4. Texture coefficient analysis of all unconverted Ti samples calculated from relative intensity values and X-ray diffraction peak data.

detected (most notable being the Na 1s at *ca.* 1071 eV and Na KLL Auger peak at *ca.* 498 eV), with significant increase in intensity of the Ti LMM peaks, which overlap with Na 1s spectra.

Concerning the high-resolution spectra, noticeable differences in the O 1s peak (Fig. 5B) deconvolutions and subsequent positions were identified. The 316L SS control peak contained 3 constituent peaks located at 530.1 (39.0%), 531.6 (48.9%), and 533.1 (12.1%) eV, corresponding to O^{2-} ($M^{x+}O_x$; M = Cr, Fe, etc.), OH^- ($M^{x+}(OH)_x$; M = Cr, Fe, etc.), and H_2O chemical states. For the Ti coated samples, the three constituent peaks remained with similar peak positions, however, their relative proportions differed; O^{2-} (79.1 ± 0.7%; Ti^{4+}—O), OH^-/defective oxides (15.6 ± 0.5%; hydroxides/Ti^{3+}—O/Ti^{2+}—O), and H_2O (5.3 ± 0.5%). Following titanate conversion, an additional constituent peak appeared at *ca.* 535.2 eV, which matched the Na KLL Auger peak. Again all other peaks remained in their position at 530.0, 531.7, and 533.1 eV corresponding to O^{2-} (75.2 ± 0.4%; Ti^{4+}—O), OH^- (11.6 ± 0.4%; hydroxides), and H_2O (5.3 ± 0.6%; experiencing a subtle shift). Variations in the relative intensities were noted as above for the Ti coated samples, with lower proportions of the OH^-/defective oxide (15.6 ± 0.5%) photoelectron peak.

For the Ti 2p doublet deconvolutions (Fig. 5C), there was a clear alteration in the number of constituent peaks following titanate conversion of the produced Ti films. Initially, the Ti coated samples contained Ti in 4 different valence states; Ti^{4+} (69.9 ± 1.5%; 2p3/2 = *ca.* 458.6 eV), Ti^{3+} (9.9 ± 0.5%; 2p3/2 = *ca.* 457.1 eV), Ti^{2+} (4.5 ± 0.2%; 2p3/2 = *ca.* 455.3 eV), and Ti^0 (15.7 ± 1.1%; 2p3/2 = *ca.* 453.4 eV), representing different titanium oxide and hydroxide states (TiO, Ti_2O_3 and TiO_2) as well as metallic titanium. Post-titanate conversion, the number of constituent peaks dropped to only contain Ti in its 4^+ valence state (2p3/2 = *ca.* 458.4 eV).

In the high-resolution spectra of the range for Na 1s (Fig. 5D), a peak was present in both the pre- and post-titanate converted samples, however, this was due to the overlapping of the Ti LMM Auger peaks with the Na 1s spectrum. The intensity of the peak increased for the titanate converted samples, demonstrating a peak at *ca.* 1071.4 eV, quantified as Na 1s (Na—O; 56.6 ± 6.9%).

3.1.5. Raman spectroscopy

As seen in Fig. 6A, there are clear differences in peak positions from the pre-treated samples, to the titanate converted films. For all pre-treated samples, the peaks presented were all attributed

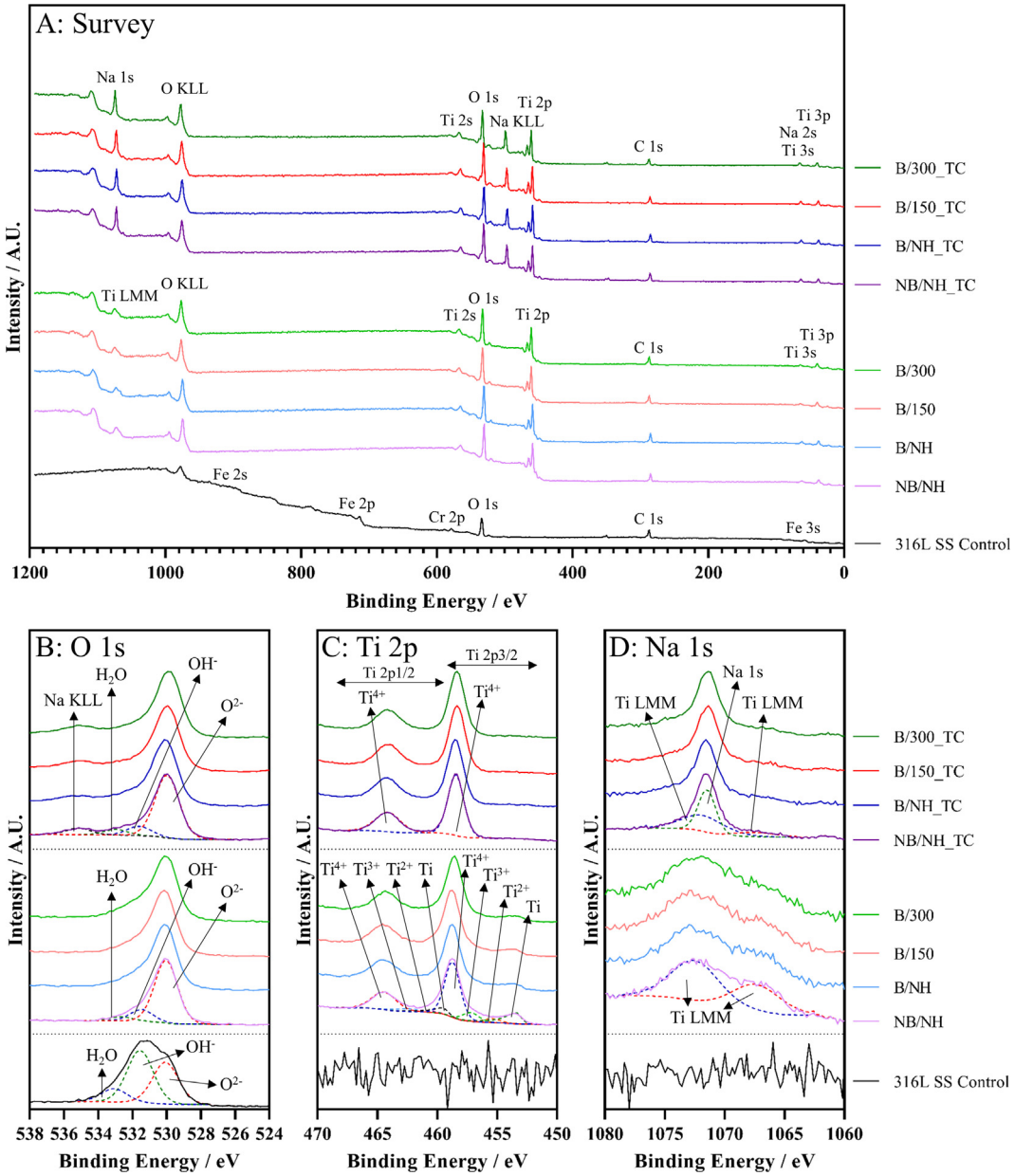

Fig. 5. X-ray photoelectron spectral analysis for control, Ti coated and titanate converted samples. (A) Survey spectra identifying all elemental photoelectron emissions, (B) High-resolution spectra of O 1s peaks with overlapping Na KLL Auger emission, (C) High-resolution spectra of Ti 2p doublet splitting peaks, and (D) High resolution spectra of Na 1s, with overlapping Ti LMM Auger emissions.

to TiO_2 with anatase phases in the lower Raman shifts (<300 cm^{-1}). Following NaOH treatment, alternate peaks at 285, 440, and 900 cm^{-1}, with broad peaks around 630–690 cm^{-1} were delineated as a form of sodium hydrogen titanate ($Na_xH_{2-x}Ti_3O_7$).

3.1.6. Fourier transform infrared spectroscopy (FTIR)

The FTIR spectrum for all converted titanate samples is shown in Fig. 6B. The unconverted Ti films did not present any discernible peak from the background measurements and, therefore, have not been shown. The broad band between 3000 and 3500 cm^{-1} is attributable to fundamental O—H stretching groups of chemisorbed water. Additionally, there may be peaks consistent with Ti interaction with —OH groups contained within this broad peak. The peak at 1650 cm^{-1} is also related to O—H bonding. The doublet peak located at 1410 and 1440 cm^{-1} is characteristic of C—H deformations of adventitious carbon and the peaks present between 850 and 900 cm^{-1} are attributable to Ti—O and Ti—O—Ti bonding, which when factored with the previously mentioned peaks points toward titanate formation.

3.1.7. Optical profilometry

To determine sample topography and roughness, optical profilometry was utilised. Sample roughness data *via* optical profilometry was detailed in Fig. 7. It is clear that the polished SS substrate exhibited a reduction in surface roughness (S_a = 129 nm for Control, which reduced to <40 nm) following sputtering of the Ti films. The roughness of the samples then increased significantly from *ca.* 23.5, 40.0, 27.9, and 35.8 nm to 140.6, 94.4, 90.4, and 52.6 nm, for the NB/NH, B/NH, B/150, B/300, and NB/NH_TC, B/NH_TC, B/150_TC, and B/300_TC samples, respectively, with the exception of B/300 (whose S_a only subtly increased), following titanate conversion (B/300_TC).

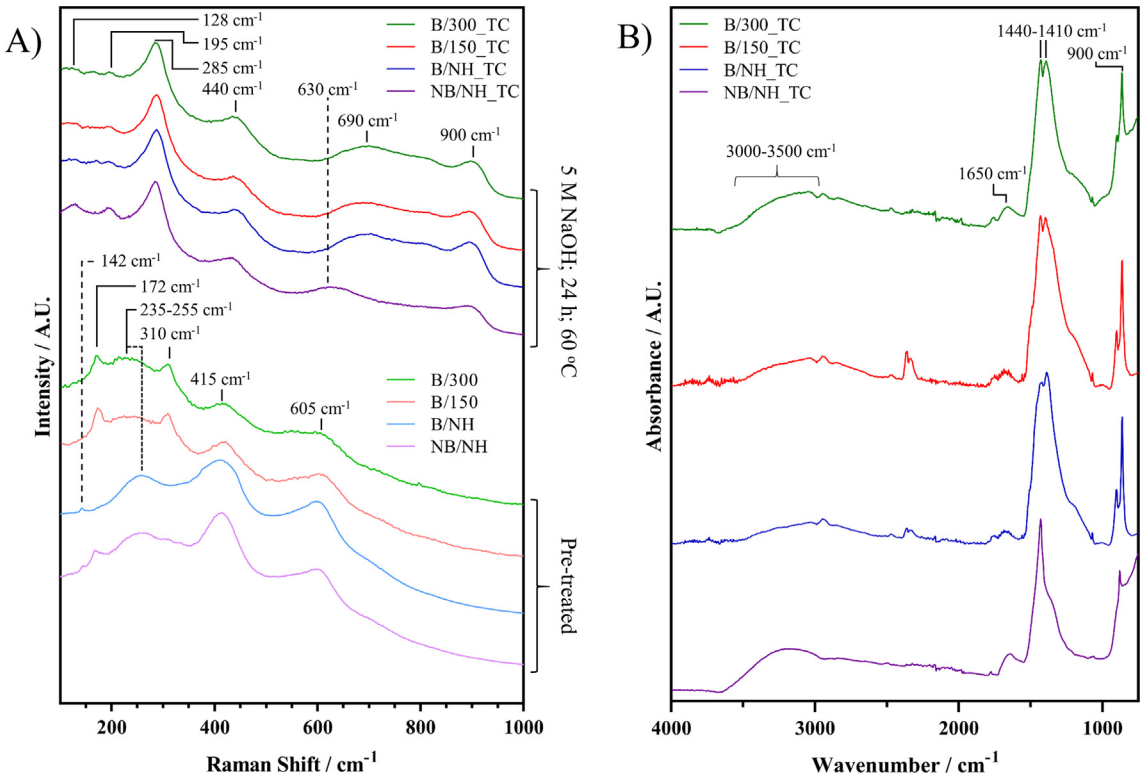

Fig. 6. (A) Raman spectral data for both unconverted and converted Ti films. (B) FTIR data of converted Ti films; Note all unconverted Ti films produced no discernible peaks and, therefore, are not shown.

3.2. Mechanical testing

3.2.1. Pull off adhesion strength

Coating adhesion strength was determined using pull off adhesion testing. It was noted that through the application of a substrate bias (from NB/NH to B/NH), as well as the introduction of substrate heating (B/150 and B/300), the coating adhesion strength on the polished substrates decreased, with strengths of 42.2, 30.5, 14.5, and 5.7 MPa for the NB/NH, B/NH, B/150, and B/300 samples, respectively. Additionally, the incidence of full and partial coating failure increases with bias and substrate heating (Table 3 & Fig. 8). After subsequent titanate conversion, the coating adhesion strength significantly decreased compared to the unconverted samples, seeing a reduction from *ca.* 42 to 14 MPa for the NB/NH and NB/NH_TC samples, respectively. Similar trends are observed for all other titanate samples, with a clear reduction from the unconverted Ti samples to the titanate converted, for the same parameter type (Table 3).

3.2.2. Scratch adhesion testing

Scratch adhesion analysis was conducted as a complimentary technique to assess the relative failure loads and the associated failure modes of the produced films. It is clear there is a reduction in the required applied load to cause coating cracking and hence spallation from the NB/NH sample to the B/300 sample, as well as following titanate conversion for all sample types. Both the NB/NH and B/NH samples exhibited no spallation (L_{c3}) up to the applied 15 N load. However, the B/150 and B/300 samples exhibited spallation at *ca.* 2.9 and 1.6 N, respectively. Tensile cracking (L_{c1}) was observed for all sample types with loads of *ca.* 2.6, 2.2, 1.6, and 1.3 N for the NB/NH, B/NH, B/150, and B/300 samples, respectively, agreeing with the above trend (Table 4 & Fig. 9). Following titanate conversion, the samples were limited to ductile perforation leading to interfacial delamination. The trend between the samples is the same as that of the unconverted samples, with the NB/NH_TC sample demonstrating the highest load for spallation (L_{c3}; *ca.* 4.3 N) and the B/300_TC sample exhibiting the lowest (L_{c3}; *ca.* 1.0 N).

4. Discussion

4.1. Topographical, structural and compositional analysis

The ability to produce titanate surfaces on alternative materials through chemical conversion of Ti sputtered films, allows improved surface properties of bioinert materials, whilst also broadening the applicability of these surfaces. If appropriate bonding and optimisation of the produced films is met, these surfaces would potentially be utilised in a wide variety of applications, from hip stems, to fracture fixation devices based on metallic and non-metallic implant materials. Specifically, the broadening of this process to incorporate polymeric materials makes this technique advantageous for future biomedical applications.

By varying processing parameters, with the ultimate aim to produce denser, equiaxed films, the effects of oxygen penetration, coating microstructure and relative ingress of the NaOH solution on the formation mechanism of titanate can be explored. Structural dependency has yet to be elucidated and is critical to the results in this study. The application of a substrate bias from the NB/NH sample (5 A target current; 0 V substrate bias), to the B/NH sample (5 A target current, −100 V substrate bias), enables bombardment of the substrate by Ar^+, with sufficient energy to transfer into the produced coating. This then allows reordering of the atoms into more equiaxed structures; akin to those of bulk metallic materials. However, such a process can also cause re-sputtering of the produced coating and, therefore, optimisation of the substrate bias must be employed. In this study, optimised biasing has previously been

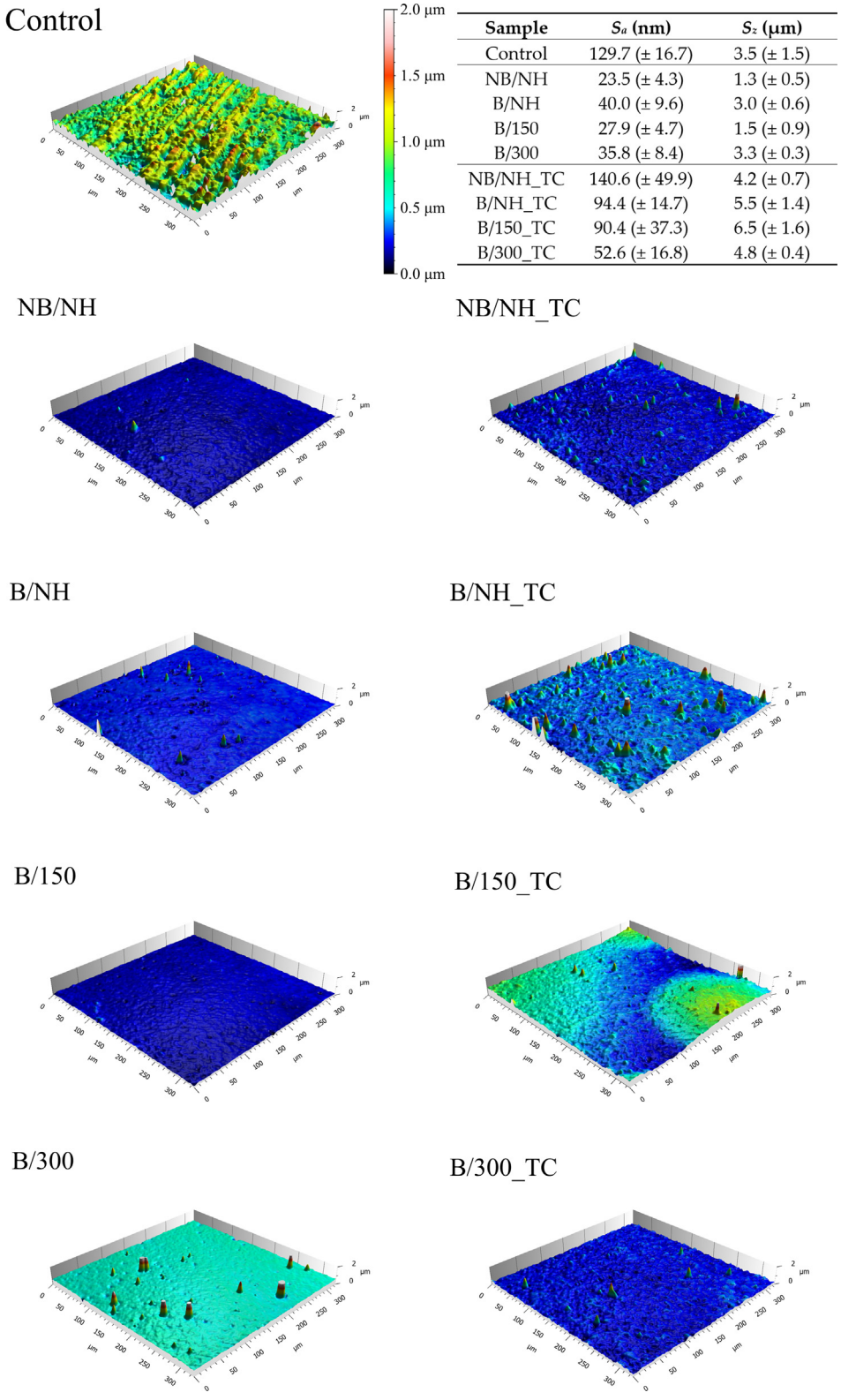

Sample	S_a (nm)	S_z (µm)
Control	129.7 (± 16.7)	3.5 (± 1.5)
NB/NH	23.5 (± 4.3)	1.3 (± 0.5)
B/NH	40.0 (± 9.6)	3.0 (± 0.6)
B/150	27.9 (± 4.7)	1.5 (± 0.9)
B/300	35.8 (± 8.4)	3.3 (± 0.3)
NB/NH_TC	140.6 (± 49.9)	4.2 (± 0.7)
B/NH_TC	94.4 (± 14.7)	5.5 (± 1.4)
B/150_TC	90.4 (± 37.3)	6.5 (± 1.6)
B/300_TC	52.6 (± 16.8)	4.8 (± 0.4)

Fig. 7. 3D visualisation and table of optical profilometry roughness values of surface topography for control, unconverted and titanate converted samples. S_a and S_z values represent arithmetic mean height and maximum height of surface features, respectively; n = 3.

determined by TEER for the rig set-up used and investigated by Priyadashini et al, with −100 V showing significant grain refinement [18]. Furthermore, application of additional surface heating in the B/150 and B/300 samples (150 °C and 300 °C, respectively) aids in energy transfer, atomic re-ordering, and, hence, its crystalline structure [19,20]. Ultimately, this understanding was confirmed in the average void area/frequency (see supplementary data Fig. S1), XRD (Fig. 3) and subsequent texture coefficient analysis (Fig. 4), with the NB/NH sample exhibiting preferred orientation in the (0 0 2) plane of HCP Ti (PDF 00-044-1294), with a T_c

Table 3
Pull off adhesion data demonstrating average failure strength of both unconverted and converted Ti films (n = 8). Additionally, the frequency of each failure mechanism has been detailed.

Sample	Failure Strength/MPa	Full Interfacial Failure	Partial Interfacial Failure	Adhesive Failure in the Epoxy
NB/NH	42.2 ± 3.5	0	5	3
B/NH	30.5 ± 3.7	2	3	3
B/150	14.5 ± 4.8	8	0	0
B/300	5.7 ± 0.6	1	6	1
NB/NH_TC	13.7 ± 2.0	4	4	0
B/NH_TC	10.8 ± 3.5	2	3	3
B/150_TC	8.1 ± 2.2	5	3	0
B/300_TC	3.0 ± 0.9	7	0	1

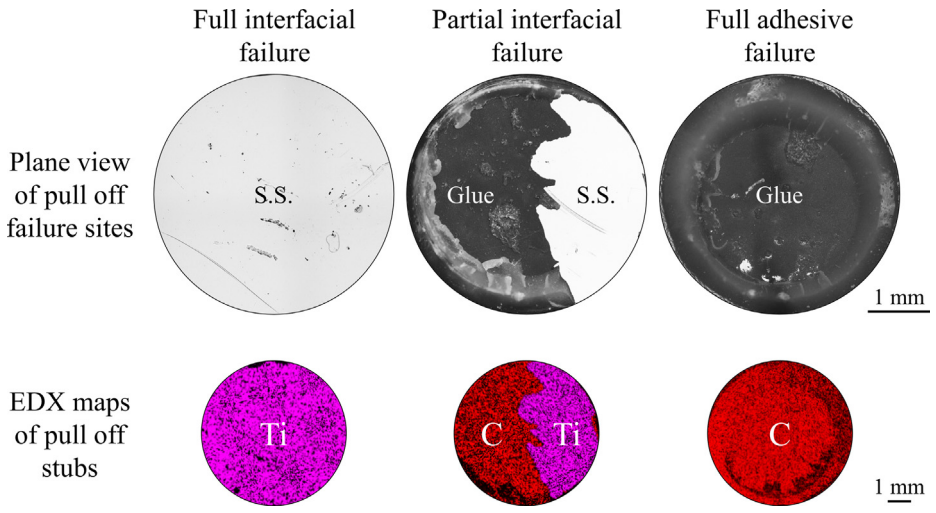

Fig. 8. Optical microscope images and EDX elemental maps of sample surfaces and pull off stubs, respectively. Typical failure modes of full interfacial, partial interfacial, and full adhesive failure shown. C elemental maps are attributed to the epoxy adhesive, whilst Ti references the failed coating.

Table 4
Failure loads calculated from failure initiation of scratch testing track profiles. Error calculated from 5 samples, in accordance with ISO 20502:2016.

Sample	Tensile Cracking (L_{c1})/N	Buckling/Chevron Cracking (L_{c2})/N	Spallation (L_{c3})/N
NB/NH	2.6 ± 0.1	9.9 ± 0.5	–
B/NH	2.2 ± 0.2	6.5 ± 0.7	–
B/150	1.6 ± 2.9	–	2.9 ± 0.4
B/300	1.3 ± 0.3	–	1.6 ± 0.5
NB/NH_TC	–	–	4.3 ± 0.4
B/NH_TC	–	–	2.3 ± 0.4
B/150_TC	–	–	1.4 ± 0.7
B/300_TC	–	–	1.0 ± 0.3

of 3.39, with the highest measured average void area (3.71 (± 0.5) × 10^{-3} μm^2), and void frequency (4.1 μm^{-2}) (see supplementary data Fig. S1); as would be expected for more columnar structures. The Ti (0 0 2) crystal plane is preferred during sputter deposition of titanium due to it being the most stable configuration for HCP structures, and has the lowest surface energy, as described by Wu et al. [21]. Both T_c and void area/frequency values decreased through the application of a bias and subsequent heating at different temperatures, with the B/300 sample exhibiting the lowest T_c (1.54; →1), void area (1.03 (± 0.2) × 10^{-3} μm^2), and void frequency (0.6 μm^{-2}) values (see supplementary data Fig. S1). These values are approaching that of bulk equiaxed Ti. The authors originally hypothesised that the more porous, columnar grown coating (NB/NH) would enable greater penetration of NaOH solution, and in turn, would cause greater conversion of the produced Ti coating, resulting in deeper titanate structure growth than the more equiaxed films (B/300). However, this was not observed in the results presented, and will be discussed as such.

SEM observations (Fig. 1) determined that the thicker titanate structures were consistent with that of the more dense, equiaxed films (B/300_TC; 1.63 μm) *vs.* the more porous, columnar structures (NB/NH_TC; 1.12 μm), however, all coating types successfully produced titanate structures similar to those already in the literature for bulk Ti [22,23]. In terms of Na inclusion in the produced titanate films, the at.% quantity remained between *ca.* 5.5 and 8.9 at.%. for the EDX measurements (Table 2), which is the average quantity over the whole e$^-$ interaction volume (*ca.* 1–2 μm penetration depth for most material types [24]; approximate penetration calculated from the Kanaya-Okayama equation [25]:

$$r(\mu\mathrm{m}) = \frac{0.0276 \cdot A \cdot E_0^{1.67}}{\rho \cdot Z^{0.89}}$$

where A is the atomic mass, Z is the atomic number, E_0 is the electron gun voltage, and ρ is the material density, r = *ca.* 1.72 μm for Ti at 15 kV). From the XPS quantity measurements (also Table 2), the more columnar structures retained more Na (25.6 and 26.8 at.% for NB/NH_TC and B/NH_TC, respectively) in the top portion of the coating (X-ray penetration for XPS on the order of a few nm; slightly higher for nanoporous titanate [24]) compared to the external heated samples (16.1 and 17.8 at.% for B/150_TC and B/300_TC, respectively); the diffusion gradient was also evident in the FIB milled sample (Fig. 2). As discussed by Zaraté et al., due to the relative ratios of contained elements quantified from the XPS analysis, the titanate composition can be correlated with obtained values from EDX. In this study, exact correlation to commonly seen titanate phases ($Na_2Ti_3O_7$ = 25 at.% Ti, 58 at.% O, 17 at.% Na;

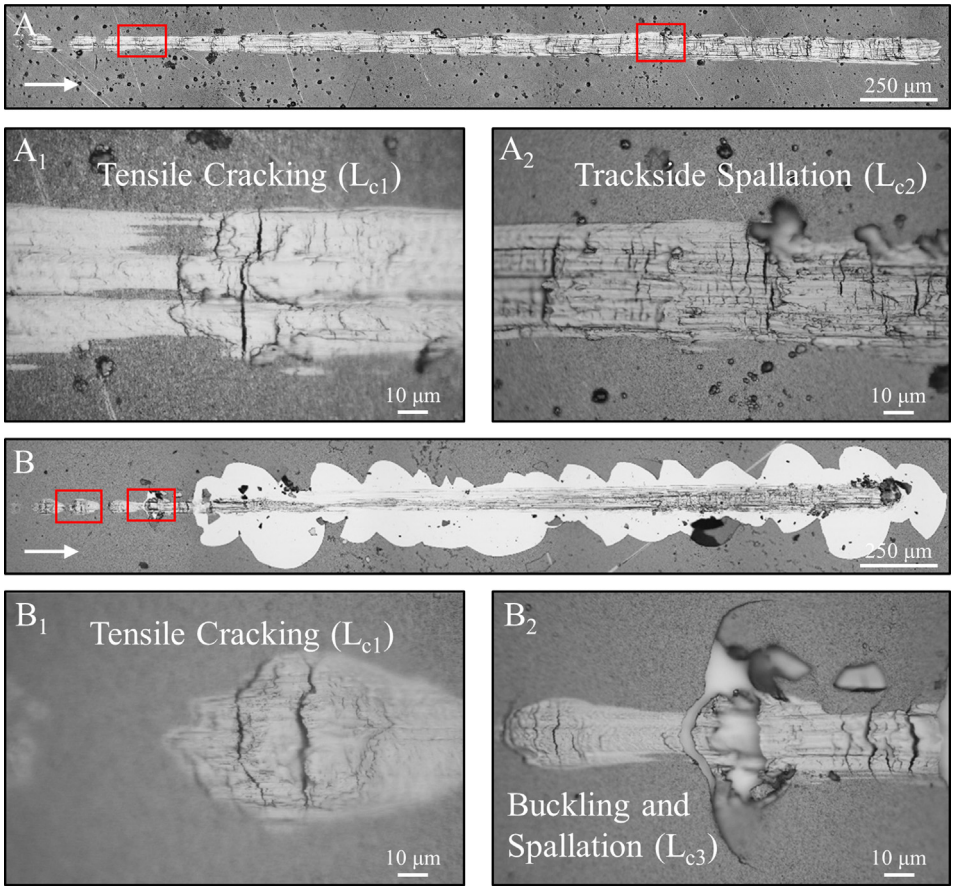

Fig. 9. Optical microscope images of typical scratch testing tracks showing the characteristic failure modes, such as tensile cracking (L_{c1}), chevron cracking (L_{c2}), and buckling/spallation (L_{c3}) denoted.

$Na_2Ti_2O_5{\cdot}H_2O$ = 17 at.% Ti, 50 at.% O, 16 at.% Na) was not possible, however, as reported by Zaraté et al., the produced titanate structure may be a mixture of closely related phases ($Na_2Ti_3O_7$; $Na_2Ti_3O_7{\cdot}nH_2O$; $Na_2Ti_2O_5{\cdot}nH_2O$), as confirmed *via* FTIR (Devi et al. [26]; Fig. 6B), XPS (Zaraté et al., Takadama et al. and others described in Takadama's paper [27,28]; Fig. 5), XRD (Devi et al. [26]; Fig. 3), and Raman (Zhang et al. & Kasuga et al. [29,30]; Fig. 6A). XRD (Fig. 3) of the titanate converted samples exhibited 3 broad peaks at *ca.* 24.2, 28.4 and 48.2° 2θ, which agreed with Devi et al., for $Na_2Ti_3O_7$, however, there is a lack of clear peaks at *ca.* 33 and 36° 2θ, which may be due to either the size of the nanocrystals/amorphous phases present, or the masking of the later peak in the (1 0 0) Ti diffraction peak [26]. A key feature is also noted with respect to the growth of the coating, since the portion of the Ti coating left on all samples following conversion is less than the original coating height (*ca.* 3.5–4 µm) produced, suggesting a two directional growth of titanate with the outwards growth being dominant; the conversion of titanium to titanate *via* diffusion results in expansion of the gel layer outwards, much like the expansion of a foam. Converse to the original hypothesis that a columnar structure would produce a thicker titanate structure *via* increased diffusion of the NaOH solution, an alternative hypothesis has been proposed by the authors. As the Ti coating transitions from a columnar to a more equiaxed structure, the fraction of voids present between the crystals reduces (*Figure S1*). As stated above, the growth of these titanate structures, produced through chemical routes, occurs perpendicular to the surface. However, in the columnar films, perpendicular growth to the crystal surface can cause growth at more oblique angles due to the presence of the voids, resulting in a thinner titanate film. The B/300 sample, being the most equiaxed and therefore containing the lowest void fraction of the films tested, produced a thicker titanate structure. The proposed phenomenon above correlates well to the observed trends of decreasing void fraction (Fig. S1) and increased titanate thickness (Fig. 1) as the Ti coating shifts from columnar (NB/NH) to more equiaxed films (B/300).

The presence of TiO_2 peaks in the Raman (Fig. 6A) spectra were to be expected since the Raman spectrometer was utilised in reflectance, hence, the thin passivated TiO_2 layer (from *ca.* 20 Å to a few nm [31–33]) would have the highest intensity. Hanaor et al. described the formation of varying phases of TiO_2, particularly noting anatase occurs in pressures less than 20 kbar and below 600 °C [34]. Therefore, the region the sputtering rig is occupying is well within this range, hence, the formation of anatase phases in the Raman spectra is logical. The broad peaks around 415 and 605 cm^{-1} are also in agreement with studies presented by Ocana et al. [35], Hsu et al. [36], and Exarhos [37]. It is worth noting the location of these peaks are similar to that of A_{1g} and E_g rutile modes, whereby Exarhos delineated that both have the same localised structural groups, however, with the additional absence of long-range order [37]. This is further noted in the XPS analysis (Fig. 5), since surface penetration is lower, whereby the produced surface layer contains multiple Ti valence states, corresponding to different titanium oxide forms (TiO_2, Ti_2O_3, and TiO). TiO_2 is the most abundant compared to Ti_2O_3 and TiO states, with the TiO being the least abundant due to thermodynamic favourability, as described by Hanawa et al. [38]. Once treated in the NaOH solution, conversion into sodium titanate was observed, with Raman peaks being noted at *ca.* 285, 440, 630–690, and 900 cm^{-1} [39–41]. The peaks at 285 and 900 cm^{-1} are in good agreement with intrinsic hydrogen titanate

($H_2Ti_3O_7$) bands found in a study conducted by Rodriguez et al. [42]. This may alternatively correspond to $Na_2Ti_3O_7$, as detailed by Bamberger et al., which revealed good agreement with the XPS and XRD analyses detailed above [43]. Furthermore, both Ma et al. and Kim et al. quantified the formation of a peak at 440 cm^{-1}, which is indicative of Ti—O bending vibrations, whereby the Ti and O atoms are 6- and 3-coordinated, respectively [44,45]. The broad peak in all TC samples ranging from 630 to 690 cm^{-1}, is characteristic of [TiO_6] octahedral Ti—O—Ti vibrations found in titanate structures, as characterised by Kasuga et al. and Zhang et al. [29,30]. These results are further confirmed from the complimentary FTIR measurements (see Fig. 6B), where Ti—O and Ti—O—Ti bonds were detected at *ca.* 850 and 900 cm^{-1}, respectively.

Cumulatively, the compositional and morphological analysis confirmed the titanate conversion of all Ti films, irrespective of the structure factor present, with the more equiaxed structure (B/300_TC) producing the thickest titanate (*ca.* 1.6 μm), demonstrating the distinct effect of the structure factor on the depth of titanate penetration.

4.2. Mechanical testing

A key consideration for any biomaterial material, which has been coated for improved surface properties, is the adherence of the produced coating, since application-dependant environments may cause fretting, micro-motion, and delamination. As determined *via* pull-off adhesion testing (Fig. 8 & Table 3), as well as coating scratch testing (Fig. 9 & Table 4), the more columnar NB/NH samples exhibited the greatest adhesion strength on the polished SS 316L samples (*ca.* 42.2 MPa, comparable to the FDA's minimum requirement of 50.8 MPa [46]), and despite cracking, did not spall during the scratch testing analysis (Fig. 9 & Table 4), proving good adhesion even on polished substrates. However, following the application of a substrate bias and substrate heating, the failure strength and spallation forces are greatly reduced. As discussed by Shen et al. (in relation to W coatings), ion-bombardment plays a significant role in the stress and microstructure of the produced coating [47]. The production of residual stresses within the coating, occurring *via* an 'atomic shot peening' effect, are higher in the denser, less columnar films, with more columnar films being unable to support large internal stresses [47]. Following titanate conversion, the respective films experienced a reduction in the adhesion strength and failure loads, which is possibly due to ingress of NaOH solution under the films, converting the bottom portion of the coating, which is exacerbated by the smooth nature of the substrate to which the coating is applied.

Despite the mechanical properties presented, the coating adhesion should increase if applied to roughened surfaces, more akin to those found on orthopaedic implants, due to the mechanical interlock present [48]. Furthermore, excessively thick coatings would not be used in practical purposes since, as determined by Vega-Morón et al. [49], the thicker the films used, the weaker the adhesion strength of the produce sputtered coating. Hence, it is clear further studies into the optimisation of these surfaces in terms of structure and thickness are needed, as well as an in-depth view on cellular proliferation/adherence and integration into surrounding tissue in *in vitro* and *in vivo* tests, respectively.

5. Conclusions

Presently, literature findings for biomedical titanates have been restricted to Ti-based substrate materials [7,8,50,51]. Despite extensive innovation and success within this research avenue, the ability to translate titanate structures to alternative materials for biomedical applications has yet to be realised within the literature. There is a clear need to produce either bioactive or antimicrobial properties on a wide range of material types for a plethora of biomedical applications. The above results have demonstrated, in detail for the first time, that translation of titanate structures onto alternative surfaces through a combinatorial DC magnetron sputtering and chemical conversion approach is possible, therefore, broadening the applicability of these surfaces for biomedical applications.

The original hypothesis of the work conducted was that variation of the structural properties of DC magnetron sputtered films would result in a higher titanate conversion percentage for columnar grown films compared to more equiaxed counterparts. However, the findings demonstrated a converse trend, whereby more equiaxed films produced the thickest titanate structures, due to the reduction in void fraction and area negating oblique angle growth of the titanate structure, which was characterised in the columnar grown films. The combination of XRD and texture coefficient analysis demonstrated the successful production of graded films from columnar, with preferred orientation in the (0 0 2) plane (NB/NH), to those more akin to equiaxed titanium (B/300). Furthermore, the titanate thicknesses produced ranged from 1.12 to 1.63 μm; thicker than currently found in the literature [51].

Optical profilometry further confirmed the increased surface roughness (S_a) values from the non-titanate converted samples (*ca.* 23–40 nm) to the titanate converted samples (*ca.* 52–140 nm). Furthermore, there was a clear trend noted in the film adherence through both the pull-off tests, as well as the scratch adhesion tests. The NB/NH sample types exhibited the greatest film strength (*ca.* 42 MPa), with decreasing values noted for the higher T_c value films (B/300 had reduced to *ca.* 6 MPa). A similar trend was also noted for the titanate converted samples, with the titanate conversion itself resulting in a decrease in film adherence compared to the native sputtered film (e.g. the NB/NH and NB/NH_TC samples exhibited pull-off failure strengths of *ca.* 42 and 14 MPa, respectively). With careful substrate surface modification through sandblasting or interlayer generation, the adhesion could be improved for these coatings making them viable for biomedical applications; currently the FDA adhesion strength standard for HA sputtered films is 50.8 MPa [46].

Currently, cellular studies are being conducted to further understand the biological impact of such coatings and to assess their efficacy for orthopaedic applications. Additional investigations into the adhesion strength of such films through the application of various interlayers and/or increased surface roughness are also being conducted, with a view to apply the titanate structures onto biodegradable materials. Ultimately, the proof of successful conversion of sputtered Ti films into titanate should open up a wide variety of material types and applications for these structures.

CRediT authorship contribution statement

Matthew D. Wadge: Conceptualization, Methodology, Validation, Investigation, Formal analysis, Resources, Data curation, Writing - review & editing, Visualization. **Burhan Turgut:** Validation, Investigation, Formal analysis, Data curation, Writing - review & editing. **James W. Murray:** Investigation, Formal analysis, Data curation, Writing - review & editing. **Bryan W. Stuart:** Conceptualization, Methodology, Supervision, Writing - review & editing. **Reda M. Felfel:** Conceptualization, Supervision, Resources, Project administration, Writing - review & editing. **Ifty Ahmed:** Conceptualization, Supervision, Project administration, Writing - review & editing. **David M. Grant:** Conceptualization, Methodology, Supervision, Funding acquisition, Resources, Project administration, Writing - review & editing.

Declaration of Competing Interest

The authors declare that they have no known competing financial interests or personal relationships that could have appeared to influence the work reported in this paper.

Acknowledgements

This work was supported by the Engineering and Physical Sciences Research Council [grant numbers EP/K029592/1, EP/L022494/1]. The authors would like to gratefully acknowledge the Nanoscale and Microscale Research Centre (nmRC) at the University of Nottingham for SEM, FEG-SEM, FIB-SEM and Raman access, in particular Dr. Chris Parmenter for FIB-SEM assistance.

Appendix A. Supplementary material

Supplementary data to this article can be found online at https://doi.org/10.1016/j.jcis.2020.01.073.

References

[1] L.A. Pruitt, A.M. Chakravartula, Mechanics of Biomaterials: Fundamental Principles for Implant Design, Cambridge University Press, 2011.
[2] J. Xu, K. Khor, Plasma spraying for thermal barrier coatings: processes and applications, in: Thermal Barrier Coatings, Elsevier, 2011, pp. 99–114.
[3] S. Dyshlovenko, B. Pateyron, L. Pawlowski, D. Murano, Numerical simulation of hydroxyapatite powder behaviour in plasma jet, Surf. Coat. Technol. 179 (2004) 110–117.
[4] L. Sun, C.C. Berndt, K.A. Gross, A. Kucuk, Material fundamentals and clinical performance of plasma-sprayed hydroxyapatite coatings: a review, J. Biomed. Mater. Res.: Off. J. Soc. Biomater. Jpn. Soc. Biomater. Aust. Soc. Biomater. Kor. Soc. Biomater. 58 (2001) 570–592.
[5] Y.-C. Yang, E. Chang, Influence of residual stress on bonding strength and fracture of plasma-sprayed hydroxyapatite coatings on Ti–6Al–4V substrate, Biomaterials 22 (2001) 1827–1836.
[6] Y. Tsui, C. Doyle, T. Clyne, Plasma sprayed hydroxyapatite coatings on titanium substrates Part 1: mechanical properties and residual stress levels, Biomaterials 19 (1998) 2015–2029.
[7] T. Kokubo, S. Yamaguchi, Novel bioactive titanate layers formed on Ti metal and its alloys by chemical treatments, Materials 3 (2010) 48–63.
[8] Y. Tian, S. Fujibayashi, S. Yamaguchi, T. Matsushita, T. Kokubo, S. Matsuda, In vivo study of the early bone-bonding ability of Ti meshes formed with calcium titanate via chemical treatments, J. Mater. Sci. – Mater. Med. 26 (2015) 271.
[9] S.K. Divakarla, S. Yamaguchi, T. Kokubo, D.-W. Han, J.H. Lee, W. Chrzanowski, Improved bioactivity of GUMMETAL®, Ti59Nb36Ta2Zr3O0. 3, via formation of nanostructured surfaces, J. Tissue Eng. 9 (2018). 2041731418774178.
[10] K. So, A. Kaneuji, T. Matsumoto, S. Matsuda, H. Akiyama, Is the bone-bonding ability of a cementless total hip prosthesis enhanced by alkaline and heat treatments?, Clin Orthopaedics Relat. Res.® 471 (2013) 3847–3855.
[11] S.-B. Lee, U. Otgonbayar, J.-H. Lee, K.-M. Kim, K.-N. Kim, Silver ion-exchanged sodium titanate and resulting effect on antibacterial efficacy, Surf. Coat. Technol. 205 (2010) S172–S176.
[12] M.D. Wadge, B.W. Stuart, K.G. Thomas, D.M. Grant, Generation and characterisation of gallium titanate surfaces through hydrothermal ion-exchange processes, Mater. Des. 155 (2018) 264–277.
[13] S. Yamaguchi, S. Nath, Y. Sugawara, K. Divakarla, T. Das, J. Manos, W. Chrzanowski, T. Matsushita, T. Kokubo, Two-in-one biointerfaces—antimicrobial and bioactive nanoporous gallium titanate layers for titanium implants, Nanomaterials 7 (2017) 229.
[14] N. Ohtsu, A. Ito, K. Saito, T. Hanawa, Characterization of calcium titanate thin films deposited on titanium with reactive sputtering and pulsed laser depositions, Surf. Coat. Technol. 201 (2007) 7686–7691.
[15] G.X. Harris, Quantitative measurement of preferred orientation in rolled uranium bars, London Edinburgh Dublin Philosoph. Mag. J. Sci. 43 (1952) 113–123.
[16] ISO, Geometrical Product Specification (GPS)–Surface Texture-Areal. Part 2: Terms, Definitions and Surface Texture Parameters, in: International Organization of Standardization, 2007, pp. 25178–25182.
[17] ASTM. Standard test method for pull-off strength of coatings using portable adhesion testers, 2009.
[18] B.G. Priyadarshini, M. Kumar Gupta, S. Ghosh, M. Chakraborty, S. Aich, Role of substrate bias during deposition of magnetron sputtered Ni, Ti and Ni–Ti thin films, Surf. Eng. 29 (2013) 689–694.
[19] M. Andritschky, F. Guimaraes, V. Teixeira, Energy deposition and substrate heating during magnetron sputtering, Vacuum 44 (1993) 809–813.
[20] H. Zhao, J. Xie, A. Mao, A. Wang, Y. Chen, T. Liang, D. Ma, effects of heating mode and temperature on the microstructures, electrical and optical properties of molybdenum thin films, Materials 11 (2018) 1634.
[21] B. Wu, Y. Yu, J. Wu, I. Shchelkanov, D.N. Ruzic, N. Huang, Y.X. Leng, Tailoring of titanium thin film properties in high power pulsed magnetron sputtering, Vacuum 150 (2018) 144–154, https://doi.org/10.1016/j.vacuum.2018.01.039.
[22] S. Yamaguchi, H. Takadama, T. Matsushita, T. Nakamura, T. Kokubo, Cross-sectional analysis of the surface ceramic layer developed on Ti metal by NaOH-heat treatment and soaking in SBF, J. Ceram. Soc. Jpn. 117 (2009) 1126–1130.
[23] H. Wang, Y.-K. Lai, R.-Y. Zheng, Y. Bian, K.-Q. Zhang, C.-J. Lin, Tuning the surface microstructure of titanate coatings on titanium implants for enhancing bioactivity of implants, Int. J. Nanomed. 10 (2015) 3887.
[24] H. Hantsche, Comparison of basic principles of the surface-specific analytical methods: AES/SAM, ESCA (XPS), SIMS, and ISS with X-ray microanalysis, and some applications in research and industry, Scanning 11 (1989) 257–280.
[25] K. Kanaya, S. Okayama, Penetration and energy-loss theory of electrons in solid targets, J. Phys. D-Appl. Phys. 5 (1972), https://doi.org/10.1088/0022-3727/5/1/308.
[26] K.B. Devi, K. Singh, N. Rajendran, Synthesis and characterization of nanoporous sodium-substituted hydrophilic titania ceramics coated on 316L SS for biomedical applications, J. Coat. Technol. Res. 8 (2011) 595.
[27] R. Zárate, S. Fuentes, J.P. Wiff, V. Fuenzalida, A. Cabrera, Chemical composition and phase identification of sodium titanate nanostructures grown from titania by hydrothermal processing, J. Phys. Chem. Solids 68 (2007) 628–637.
[28] H. Takadama, H.-M. Kim, T. Kokubo, T. Nakamura, XPS study of the process of apatite formation on bioactive Ti–6Al–4V alloy in simulated body fluid, Sci. Technol. Adv. Mater. 2 (2001) 389.
[29] T. Kasuga, M. Hiramatsu, A. Hoson, T. Sekino, K. Niihara, Titania nanotubes prepared by chemical processing, Adv. Mater. 11 (1999) 1307–1311.
[30] Z. Zhang, J.B. Goodall, S. Brown, L. Karlsson, R.J. Clark, J.L. Hutchison, I. Rehman, J.A. Darr, Continuous hydrothermal synthesis of extensive 2D sodium titanate (Na 2 Ti 3 O 7) nano-sheets, Dalton Trans. 39 (2010) 711–714.
[31] K. Aniołek, M. Kupka, A. Barylski, Characteristic of oxide layers obtained on titanium in the process of thermal oxidation, Arch. Metall. Mater. 61 (2016) 853–856.
[32] E. McCafferty, J. Wightman, An X-ray photoelectron spectroscopy sputter profile study of the native air-formed oxide film on titanium, Appl. Surf. Sci. 143 (1999) 92–100.
[33] C.J. Boxley, H.S. White, C.E. Gardner, J.V. Macpherson, Nanoscale imaging of the electronic conductivity of the native oxide film on titanium using conducting atomic force microscopy, J. Phys. Chem. B 107 (2003) 9677–9680.
[34] D.A. Hanaor, C.C. Sorrell, Review of the anatase to rutile phase transformation, J. Mater. Sci. 46 (2011) 855–874.
[35] M. Ocana, J.V. Garcia-Ramos, C.J. Serna, Low-temperature nucleation of rutile observed by raman spectroscopy during crystallization of TiO2, J. Am. Ceram. Soc. 75 (1992) 2010–2012.
[36] L. Hsu, R. Rujkorakarn, J. Sites, C. She, Thermally induced crystallization of amorphous-titania films, J. Appl. Phys. 59 (1986) 3475–3480.
[37] G.J. Exarhos, High temperature Raman studies of phase transitions in thin film dielectrics, MRS Online Proc. Library Arch. (1985,) 48.
[38] T. Hanawa, K. Asami, K. Asaoka, Repassivation of titanium and surface oxide film regenerated in simulated bioliquid, J. Biomed. Mater. Res.: Off. J. Soc. Biomater. Jpn. Soc. Biomater. Aust. Soc. Biomater. 40 (1998) 530–538.
[39] V. Prabu, P. Karthick, A. Rajendran, D. Natarajan, M. Kiran, D.K. Pattanayak, Bioactive Ti alloy with hydrophilicity, antibacterial activity and cytocompatibility, RSC Adv. 5 (2015) 50767–50777.
[40] T. Kizuki, H. Takadama, T. Matsushita, T. Nakamura, T. Kokubo, Effect of Ca contamination on apatite formation in a Ti metal subjected to NaOH and heat treatments, J. Mater. Sci. – Mater. Med. 24 (2013) 635–644.
[41] D.K. Pattanayak, T. Kawai, T. Matsushita, H. Takadama, T. Nakamura, T. Kokubo, Effect of HCl concentrations on apatite-forming ability of NaOH–HCl-and heat-treated titanium metal, J. Mater. Sci. – Mater. Med. 20 (2009) 2401–2411.
[42] V. Rodríguez-González, S. Obregón-Alfaro, L. Lozano-Sánchez, S.-W. Lee, Rapid microwave-assisted synthesis of one-dimensional silver–H2Ti3O7 nanotubes, J. Mol. Catal. A: Chem. 353 (2012) 163–170.
[43] C.E. Bamberger, G.M. Begun, Sodium titanates: stoichiometry and Raman spectra, J. Am. Ceram. Soc. 70 (1987) C-48-C-51.
[44] R. Ma, K. Fukuda, T. Sasaki, M. Osada, Y. Bando, Structural features of titanate nanotubes/nanobelts revealed by Raman, X-ray absorption fine structure and electron diffraction characterizations, J. Phys. Chem. B 109 (2005) 6210–6214.
[45] H. Kim, F. Miyaji, T. Kokubo, T. Nakamura, Effect of heat treatment on apatite-forming ability of Ti metal induced by alkali treatment, J. Mater. Sci. – Mater. Med. 8 (1997) 341–347.
[46] T.J. Callahan, J. Gantenberg, B.E. Sands, Calcium phosphate (Ca-P) coating draft guidance for preparation of Food and Drug Administration (FDA) submissions for orthopedic and dental endosseous implants, Characterization and Performance of Calcium Phosphate Coatings for Implants, ASTM International, 1994.
[47] Y. Shen, Y. Mai, Q. Zhang, D. McKenzie, W. McFall, W. McBride, Residual stress, microstructure, and structure of tungsten thin films deposited by magnetron sputtering, J. Appl. Phys. 87 (2000) 177–187.
[48] D.-M. Liu, Q. Yang, T. Troczynski, Sol–gel hydroxyapatite coatings on stainless steel substrates, Biomaterials 23 (2002) 691–698.
[49] R. Vega-Morón, G.R. Castro, D. Melo-Máximo, J. Méndez-Méndez, L. Melo-Máximo, J. Oseguera-Peña, A. Meneses-Amador, Adhesion and mechanical properties of Ti films deposited by DC magnetron sputtering, Surf. Coat. Technol. 349 (2018) 1137–1147.
[50] T. Kokubo, S. Yamaguchi, Bioactive Ti metal and its alloys prepared by chemical treatments: state-of-the-art and future trends, Adv. Eng. Mater. 12 (2010) B579–B591.
[51] T. Kokubo, S. Yamaguchi, Biomineralization of metals using chemical and heat treatments, in: Biomineralization and Biomaterials, Elsevier, 2016, pp. 339–364.